Journal of Science: Advanced Materials and Devices 10 (2025) 100934

Contents lists available at ScienceDirect

Journal of Science: Advanced Materials and Devices

journal homepage: www.elsevier.com/locate/jsamd

Research Article

Lightweight and broadband NiO/Ni/borophene foams for enhanced electromagnetic wave attenuation

Wala Dizayee [a,b], Mohammed Ahmed Mohammed [c], Mohammed Zorah [d,e], HassabAlla M.A. Mahmoud [f], Mohamed Shabbir Abdulnabi [g,*], G. Abdulkareem-Alsultan [h,j,**], Maadh Fawzi Nassar [i,j,***]

[a] Department of General Sciences, College of Basic Education, Salahaddin University-Erbil, Erbil, Kurdistan Region, Iraq
[b] Department of Pharmacy, College of Pharmacy, Knowledge University, Erbil, Kurdistan Region, Iraq
[c] Department of Soil Science and Water Resources, College of Agriculture, University of Al-Qadisiyah, Al-Qadisiyah, Iraq
[d] Department of C. T. E, Imam Alkadhim University College, Baghdad, Iraq
[e] Mazaya University College, Thi Qar, 64001, Iraq
[f] Department of Physics, Applied College, King Khalid University, Muhayil, 61913, Saudi Arabia
[g] School of Technology, Asia Pacific University of Technology and Innovation (APU), 57000, Kuala Lumpur, Malaysia
[h] Catalysis Science and Technology Research Centre, Faculty of Science, Universiti Putra Malaysia, Serdang, 43400, Malaysia
[i] Integrated Chemical Biophysics Research, Faculty of Science, Universiti Putra Malaysia, 43400, UPM Serdang, Selangor, Malaysia
[j] Department of Chemistry, Faculty of Science, Universiti Putra Malaysia, UPM Serdang, Selangor, 43400, Malaysia

ARTICLE INFO

Keywords:
Borophene
NiO/Ni/borophene
Nanocomposites
Electromagnetic

ABSTRACT

The development of high-performance microwave absorbing materials poses a significant challenge due to the complex balance required between dielectric and magnetic losses, structural integrity, and impedance matching. Conventional NiO/Ni composites, though promising, face several limitations Nickel demonstrates significant magnetic loss but inadequate impedance matching, whereas nickel oxide, functioning as a dielectric, provides minimal attenuation and restricted conductivity. Moreover, particle aggregation, elevated material density, and limited absorption bandwidth further constrain their utility in contemporary electromagnetic interference (EMI) shielding systems. This study presents a unique 3D hierarchical NiO/Ni/Borophene (NNB) nanocomposite synthesized by a scalable, solution-based method to address these inherent limitations. Borophene, a lightweight, metallic, and anisotropically conductive two-dimensional substance, serves as a structural and functional enhancer. Its integration accelerates charge transport, increases dielectric loss through interfacial polarization, and facilitates impedance matching by reducing excessive conductivity. The freeze-dried design presents a foam-like structure that enhances multiple scattering and effectively attenuates incident waves. Of the compositions analyzed, NNB-20 (20 wt % borophene) demonstrated superior performance, with a minimum reflection loss of −55.5 dB at 12.8 GHz and a wide absorption bandwidth. This study emphasizes borophene's synergistic roles in overcoming the limitations of traditional NiO/Ni systems, establishing NNB nanocomposites as a novel category of lightweight, broadband, and high-efficiency microwave absorbers for sophisticated EMI shielding applications.

1. Introduction

The rapid proliferation of electromagnetic (EM) technologies in communication, radar, and electronic gadgets has heightened the necessity for sophisticated microwave-absorbing materials that can alleviate electromagnetic interference (EMI) and pollution [1–4]. Optimal absorbers must integrate lightweight construction, extensive bandwidth, robust absorption, and structural integrity; nonetheless,

* Corresponding author.
** Corresponding author. Catalysis Science and Technology Research Centre, Faculty of Science, Universiti Putra Malaysia, Serdang, 43400, Malaysia.
*** Corresponding author. Integrated Chemical Biophysics Research, Faculty of Science, Universiti Putra Malaysia, 43400 UPM Serdang, Selangor, Malaysia.
E-mail addresses: mohamed.shabbir@apu.edu.my (M.S. Abdulnabi), kreem.alsultan@yahoo.com (G. Abdulkareem-Alsultan), nassarmaadh@gmail.com (M.F. Nassar).

https://doi.org/10.1016/j.jsamd.2025.100934
Received 13 April 2025; Received in revised form 19 May 2025; Accepted 13 June 2025
Available online 19 June 2025

attaining this synergy continues to pose a significant problem [5,6]. Conventional materials, such as ferrites and carbon-based composites, frequently prove inadequate due to their elevated density, restricted tunability, or inadequate attenuation over broad frequency ranges [5–12]. Recent advancements in nanotechnology and two-dimensional (2D) materials have created new opportunities for the development of next-generation absorbers, utilizing their extensive surface area, adjustable electrical characteristics, and compatibility with hierarchical structures to improve electromagnetic wave dissipation [13–24] (see Scheme 1).

Heterostructured composites that incorporate metal oxides, metallic phases, and two-dimensional materials have emerged as viable options. Nickel oxide (NiO), a p-type semiconductor exhibiting dielectric characteristics, combined with metallic nickel (Ni) in a heterojunction, illustrates this methodology by integrating dielectric loss with magnetic effects to enhance impedance matching and absorption efficiency. NiO/Ni systems, when supported on porous carbon, have exhibited the capability to produce urchin-like morphologies that enhance wave scattering and interfacial polarization [25–30]. Likewise, 2D materials such as MXenes (e.g., $Ti_3C_2T_x$) have garnered interest due to their metallic conductivity, surface functionality, and capacity to immobilize magnetic or dielectric nanoparticles, resulting in multi-phase composites with improved electromagnetic attenuation [31–33]. These composites frequently utilize flower-like or foam-like architectures to enhance porosity and interaction with incident waves, attaining reflection losses as little as −50 dB in the gigahertz spectrum [34–37]. Inspired by these findings, the integration of borophene into such a heterostructure presents an unexplored yet highly promising avenue for next-generation electromagnetic wave shielding materials [38–41].

Borophene, a novel two-dimensional substance comprised of boron atoms, offers a new perspective in this domain [42–44]. In contrast to graphene or MXenes, borophene presents a distinctive amalgamation of metallic conductivity, minimal weight, and structural anisotropy, rendering it an attractive option for electromagnetic applications [45,46]. Although its incorporation into functional composites is less investigated than other 2D materials, initial research on borophene-functionalized magnetic nanoparticles indicates its potential to improve charge transport and interfacial interactions [47–49]. Integrating borophene with NiO/Ni heterojunctions in a three-dimensional (3D) configuration may provide synergistic loss mechanisms—dielectric from NiO, magnetic from Ni, and conductive from borophene—while utilizing a hierarchical structure to enhance wave trapping and dissipation. This work presents a new 3D hierarchical NiO/Ni/Borophene nanocomposite engineered for enhanced microwave absorption. In contrast to traditional methods that depend on expensive vapor-phase procedures, we suggest a scalable, solution-based approach utilizing hydrothermal synthesis and liquid-phase exfoliation, succeeded by freeze-drying to maintain the three-dimensional architecture [50]. This approach utilizes adjustable foam-like structures by integrating borophene as a lightweight, conductive enhancer. The resultant nanocomposite seeks to overcome the constraints of current absorbers—namely, elevated density or restricted bandwidth—by providing a porous, multi-interface architecture that optimizes polarization, conduction, and scattering losses [51,52]. This research broadens the utilization of borophene in electromagnetic materials and reconfigures the design of hierarchical composites, facilitating the development of lightweight, high-performance microwave absorbers suited to contemporary technical requirements.

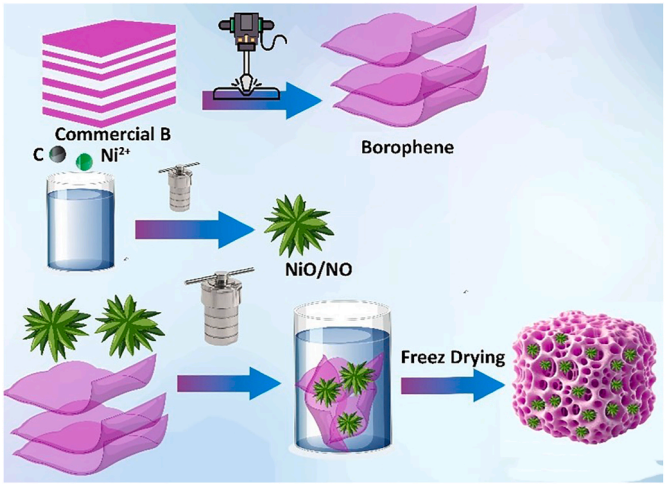

Scheme 1. Schematic preparation process of NNCBs composites.

Integrating borophene into 3D hierarchical NiO/Ni/Borophene nanocomposite for enhanced microwave absorption presents significant benefits compared to more prevalent 2D materials such as MXenes (e.g., $Ti_3C_2T_x$) or graphene [53,54]. The benefits arise from borophene's distinctive structural, electrical, and physical characteristics, such as ultralight weight, metallic conductivity with anisotropy, higher surface area and structural flexibility. Borophene, composed of boron atoms (atomic mass ~10.81 u), is lighter than graphene (carbon, ~12.01 u) and considerably lighter than MXenes (containing heavy metals as titanium (~47.87 u) in Ti_3C_2T low density (~2.3 g/cm^3 vs. ~2.2 g/cm^3 for graphene and ~4–5 g/cm^3 for MXenes) decreases the weight of the NiO/Ni/Borophene composite as well as this, Unlike graphene (isotropic semi-metal) and MXenes (metallic, termination-moderated), borophene's puckered lattice makes it metallic with anisotropic conductivity, allowing adjustable charge transport along particular directions [42,55–57]. In a 3D hierarchical structure, borophene's anisotropic conductivity could match electron routes with incident EM waves, increasing conductive loss and outperforming graphene or MXenes. Tunability may enhance impedance matching and absorption bandwidth [58–61].

2. Experimental

2.1. Chemicals and materials

Nickel (II) chloride hexahydrate ($NiCl_2{\cdot}6H_2O$, 98 %), urea ($CO(NH_2)_2$, 99 %), sodium borohydride ($NaBH_4$, 98 %), magnesium diboride (MgB_2, 99 %), N-methyl-2-pyrrolidone (NMP, 99.5 %), polyvinylpyrrolidone (PVP, MW ≈ 40,000), isopropyl alcohol (IPA, 99.8 %), ethylene glycol (EG, 99 %), and porous carbon (specific surface area ~500 m^2/g, pore size ~10–50 nm) were acquired from Sigma-Aldrich. Deionized water (DIW, resistivity 18.2 MΩ cm) served as the solvent unless specified differently. All reagents were of analytical quality and utilized without additional purification.

2.2. Synthesis of NiO/Ni on porous carbon

The NiO/Ni heterostructure was prepared via a solvothermal technique, thereafter undergoing partial reduction. In a standard process, 1.19 g of $NiCl_2{\cdot}6H_2O$ (0.1 M) and 0.60 g of urea (0.2 M) were dissolved in 50 mL of ethylene glycol under vigorous agitation at ambient temperature for 30 min until a clear green solution was obtained. Subsequently, 0.5 g of porous carbon was introduced into the solution and subjected to ultrasonication (100 W, 40 kHz) for 15 min to achieve uniform dispersion. The suspension was placed in a 100 mL Teflon-lined stainless-steel autoclave, sealed, and held at 175 °C for 14 h in an electrically heated oven. Upon natural cooling to room temperature, the black precipitate (NiO/porous carbon) was harvested using centrifugation (5000 rpm, 10 min), rinsed thrice with DI water and ethanol, and then vacuum-dried at 80 °C for 14 h. To create the NiO/Ni heterojunction, 0.5 g of dried NiO/porous carbon was suspended in 50 mL of deionized water, and 0.19 g of $NaBH_4$ (0.05 M) was gradually introduced while stirring at 25 °C for 1 h. The resultant NiO/Ni/porous

carbon was filtered, washed with DI water till reaching neutral pH, and afterward dried at 60 °C for 6 h under vacuum conditions.

2.3. Synthesis of borophene nanosheets

Borophene nanosheets were produced from boron crystal powder by a liquid-phase exfoliation technique. Initially, 1 g of high-purity boron powder was suspended in 100 mL of N-methyl-2-pyrrolidone (NMP), to which 0.1 g of polyvinylpyrrolidone (PVP) was incorporated as a stabilizing agent to inhibit nanosheet agglomeration. The mixture underwent high-power ultrasonication (500 W, 40 kHz) in an ice bath for 6 h. The sonication procedure supplied adequate energy to surpass the interatomic forces in bulk boron, facilitating the delamination and exfoliation of few-layer borophene sheets. Following exfoliation, the dispersion was subjected to centrifugation at 3000 rpm for 20 min to eliminate unexfoliated particles, and the resultant clear supernatant containing borophene nanosheets was collected. The nanosheets were redispersed in 50 mL of isopropyl alcohol using mild sonication (100 W, 40 kHz) for 10 min to enhance dispersion and compatibility. The resultant borophene dispersion, with an estimated concentration of around 4 mg/mL, exhibited stability and was appropriate for incorporation into nanocomposite structures.

2.4. Development of 3D hierarchical NiO/Ni/borophene nanocomposite

The 3D hierarchical NiO/Ni/borophene nanocomposite was synthesized by a solution assembly and freeze-drying technique. 0.5 g of NiO/Ni/porous carbon powder was suspended in 20 mL of deionized water under magnetic agitation for 30 min 50 mL of borophene dispersion (~0.2 g borophene in isopropyl alcohol) were added dropwise to the NiO/Ni suspension, and the mixture was agitated at ambient temperature for 2 h to ensure homogenous integration. The resultant slurry was transferred into a cylindrical Teflon mold (diameter 5 cm, height 2 cm) and promptly frozen in liquid N2 (−196 °C) for 10 min to stabilize the structure. The solidified material was subsequently placed in a freeze-dryer (Labconco FreeZone) and lyophilized at −50 °C and 0.1 mbar for 48 h. The ultimate product, a lightweight 3D hierarchical NiO/Ni/borophene nanocomposite, was acquired in the form of a porous monolith. Samples with different borophene concentrations were created by modifying the volume of borophene dispersion to attain 0 wt %, 20 wt %, and 40 wt % borophene in relation to NiO/Ni, designated as NNB-0, NNB-20, and NNB-40, respectively.

2.5. Characterization of materials

The crystalline phases of the nanocomposite were examined via X-ray diffraction (XRD, Rigaku D/Max-2500, Cu Kα radiation, $\lambda = 1.5406$ Å) at a scanning rate of 5°/min over the range of 10°–80° 2θ. The morphology and microstructure were examined using field-emission scanning electron microscopy (FE-SEM, Hitachi S-4800) and transmission electron microscopy (TEM, JEOL JEM-2100F), which included energy-dispersive X-ray spectroscopy (EDS) for elemental mapping. The chemical composition and bonding states were analyzed using X-ray photoelectron spectroscopy (XPS, Kratos Axis Ultra DLD) with an Al Kα source. The specific surface area and pore structure were ascertained by nitrogen adsorption-desorption isotherms (Micromeritics ASAP 2020) utilizing the Brunauer-Emmett-Teller (BET) and Barrett-Joyner-Halenda (BJH) methodologies.

2.6. Electromagnetic performance evaluation

The nanocomposite samples were combined with paraffin wax at a filler loading of 30 wt % (70 wt % paraffin), heated to 80 °C, and molded into toroidal rings with an external width of 7.0 mm, an internal width of 3.04 mm, and a depth of about 2 mm to evaluate microwave absorption capabilities. Electromagnetic characteristics, comprising complex permittivity ($\varepsilon\_r = \varepsilon' - j\varepsilon''$) and permeability ($\mu\_r = \mu' - j\mu''$), were assessed utilizing a vector network analyzer (Agilent N5230A) across the frequency spectrum of 2–18 GHz. Reflection loss (R_L) was determined utilizing transmission line theory, employing the measured ε_r and μ_r values for sample thicknesses between 1.0 and 5.0 mm.

3. Result and discussion

The SEM in Fig. 1 provides insights into the morphological characteristics of the 3D hierarchical NiO/Ni/borophene (NNB) foam, emphasizing its interconnected architecture, porous configuration, and surface properties. The highly porous nature facilitates multiple scattering effects for electromagnetic wave absorption. The pink arrows highlight NiO/Ni nanoparticles anchored on borophene nanosheets, forming a heterostructure interface. The porous 3D B exhibited numerous voids, with the majority of the monolayer B oriented in the direction of water crystallization following freeze-drying. 2D B interlaced to create a 3D network. The monolayer B can intersect in a three-dimensional configuration or on a planar surface. The diverse, overlapping techniques effectively endowed B with a three-dimensional architecture resembling a permeable scaffold. Fig. 1c demonstrates that, alongside the holes in the parallel orientation, there were also pores in the vertical orientation resulting from minimal overlap between B layers. The three-dimensional structured framework formed by 2D B resulted in the distribution of NiO (shown by the pink arrows in Fig. 1d) on its surface.

The geometry and crystalline arrangement of the NiO/Ni/C-Borophene (NNCB) composite are examined using TEM, HRTEM, and SAED characterizations, as illustrated in Fig. 2. The TEM images of NiO-Borophene (Fig. 2a) and Ni-Borophene (Fig. 2d) demonstrate that the NiO and Ni nanoparticles are roughly 9 nm in diameter and are uniformly dispersed throughout the borophene nanosheets. The borophene structure in both composites displays a distinct and well-defined border, facilitating an increased surface-to-volume ratio for the dispersion of NiO/Ni nanoparticles. Moreover, borophene's inherent high electrical conductivity promotes efficient electron transport, hence improving the composite's total conductivity. The HRTEM pictures of NiO-Borophene (Fig. 2b) and Ni-Borophene (Fig. 2e) exhibit a uniformly aligned lattice patterns, indicative of crystalline NiO and Ni, respectively. The interplanar spacing of the (111) face of NiO is 0.241 nm, indicative of its cubic phase (space group: Fm-3m (225), PDF card no. 47–1049), as evidenced by the HRTEM image of NiO. The interlayer spacing of the (111) plane of Ni is 0.203 nm, aligning with its face-centered cubic (FCC) structure (space group: Fm-3m (225), PDF card no. 04–0850). The SAED patterns of NiO and Ni are presented in Fig. 2c and f, respectively. The circular diffraction patterns match with the (111), (200), (220), (311), and (222) facets of NiO, which are in agreement with the NiO's X-ray diffraction pattern (Fig. 3b). Similarly, the (111), (200), and (220) planes of Ni match the observed SAED diffraction circles, confirming their consistency with the XRD results of Ni (Fig. 3b). These findings validate the successful synthesis of NNBcomposites, ensuring the formation of a well-integrated NiO/Ni heterostructure on borophene. For validating consistent distribution" of NiO and Ni on the borophene nanosheets, TEM-EDS elemental mapping was conducted, as illustrated in Fig. 2g–j. The dark field images of NiO-Borophene (NNB–O) and Ni-Borophene (NNB–Ni), combined with the respective elemental maps for Ni, O, and B, demonstrate that NiO and Ni nanoparticles are homogeneously dispersed throughout the borophene framework.

The EDS of NNB-40 analysis additionally differentiates between NiO and Ni phases. The atomic ratio of O in NNB-O and NNB-Ni were determined to be 25.2 % and 36.2 %, respectively. The results validate the effective synthesis of the 3D NiO/Ni-Borophene heterostructure.

The phase composition of the Bulk B, exfoliated borophene, and 3D hierarchical NiO/Ni/Borophene nanocomposites (NNB-0, NNB-20, NNB-40) was confirmed by X-ray diffraction (XRD) [34]. The XRD pattern of bulk boron is distinguished by strong peaks within the

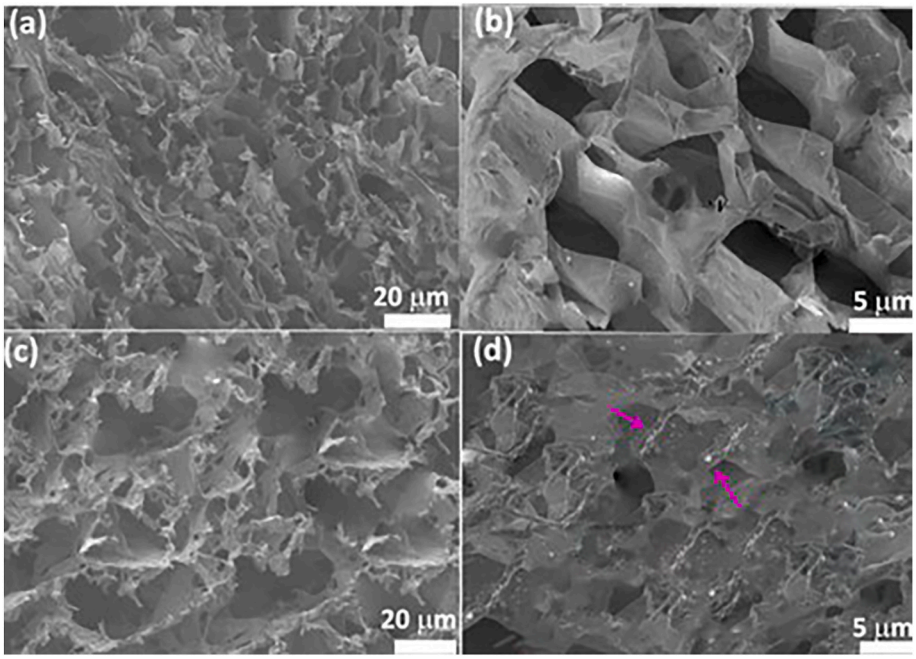

Fig. 1. SEM pictures of (a) 3D porous borophen, (b) framed structure, (c) wall pores, and (d) 3D porous NNB heterostructure at a mass fraction of 2:1.

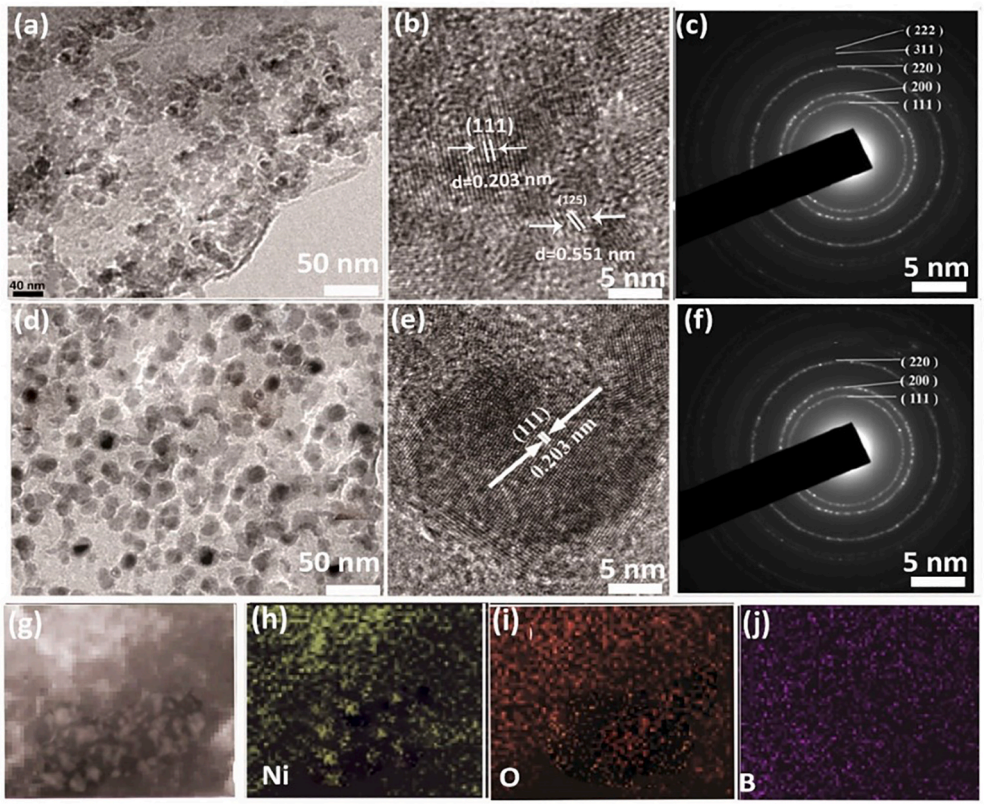

Fig. 2. (a) TEM images of NiO/B, (b) HRTEM image of NiO/B (c) Selected-area diffraction (SAED) of NiO/B (d) TEM images of Ni/B (e) HRTEM image of Ni/B (f) SAED of SAED (g–j) EDS mapping of NNCB-40.

10°–80° 2θ range. Significant peaks are detected at roughly 27.8°, 41.8°, 50.2°, 62.3°, and 74.5° 2θ, corresponding to the rhombohedral β-rhombohedral boron structure (PDF#31–0207) (Fig. 3a) [62,63]. The pronounced peaks signify a highly crystalline, three-dimensional lattice characteristic of bulk boron materials, exhibiting long-range order and few defects. The liquid-phase exfoliated pattern exhibits a notable decrease in peak intensity and a broad, diffuse characteristic between 20° and 30° 2θ, with very slight residual peaks at elevated angles. The extensive peak indicates a reduction in long-range crystallinity, aligning with the development of few-layer or amorphous borophene nanosheets. The reduced intensity and absence of sharp reflections signify effective exfoliation, wherein the layered architecture of the precursor (e.g.,

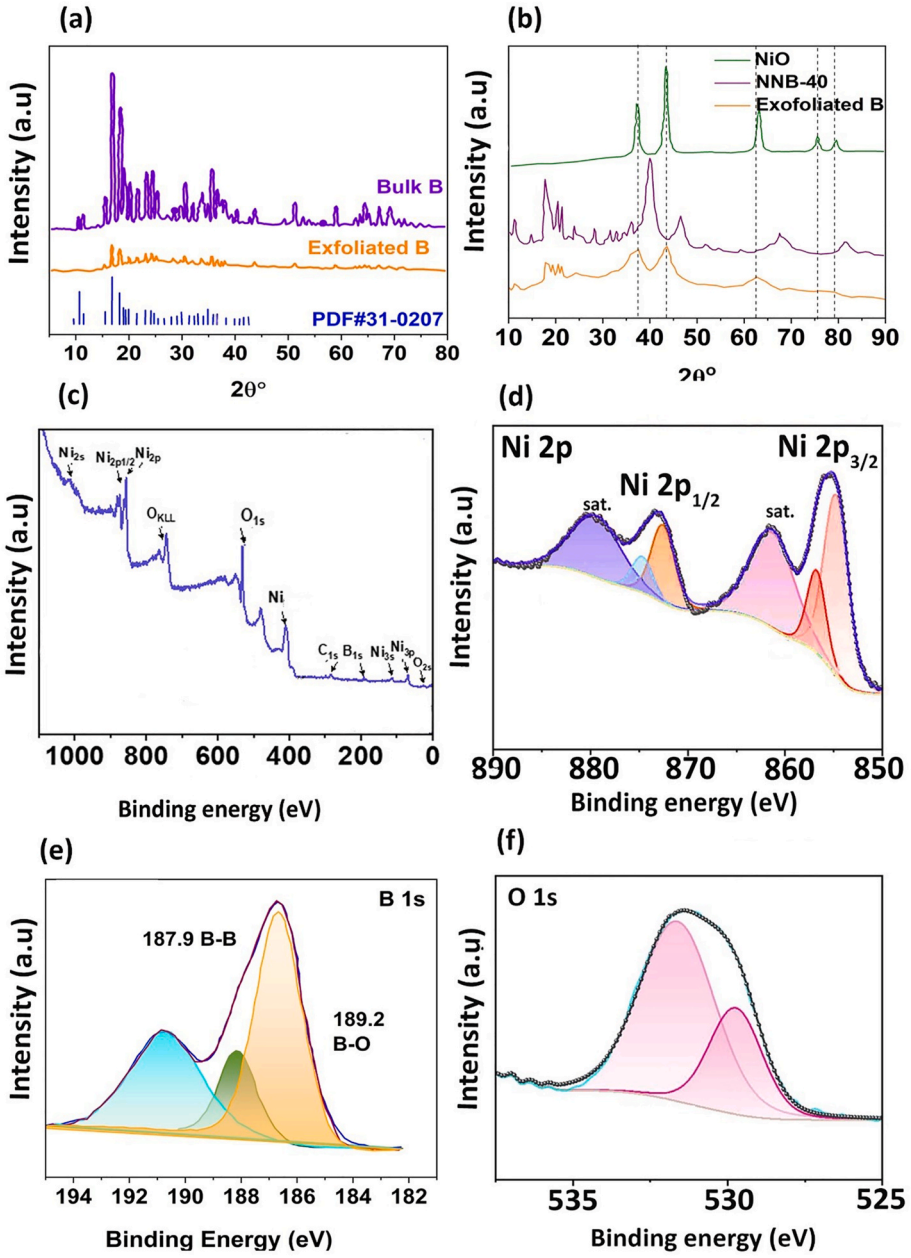

Fig. 3. (a) XRD pattern of commercial B and exfoliated B, (b) XRD pattern exfoliated B, NiO and NNB-40, (c) XPS survey spectra of NNB-40, (d)High -resolution deconvoluted XPS spectra of (d) Ni 2p; (e) B 1s; (f) O 1s.

MgB_2) has been fragmented into thinner, less organized sheets. Fig. 3b depicts NiO, exfoliated boron (exfoliated B), and a NiO@B (NNB) composite, with an additional reference to B_2O_3. The pronounced peaks signify a highly crystalline structure, characteristic of NiO produced by solvothermal processes, as outlined in our experimental procedure. The peak at 43.3° is notably pronounced, indicating the robust (200) reflection. The XRD pattern of NBB retains the principal NiO peaks (e.g., 37.2°, 43.3°, 62.9° 2θ) with somewhat diminished intensity, signifying that the NiO crystalline structure remains predominant [62,64]. Furthermore, a prominent characteristic akin to exfoliated B emerges between 20° and 30° 2θ, corroborating the existence of borophene in the composite. The intersection of NiO and borophene signals indicates a potential physical or chemical interaction, possibly including the coating or integration of borophene onto NiO surfaces. The relative intensity of the borophene characteristic is diminished compared to the pure exfoliated B pattern, perhaps due to dilution by the NiO matrix [49,65,66].

To analyze the chemical composition, oxidation states, and surface interactions within the NiO/Ni-Borophene (NNB) composite, XPS spectra were collected, as shown in Fig. 3c–f. The survey and high-resolution spectra elucidate the oxidation states of Ni, B, and O, thereby validating the effective synthesis of the NiO/Ni-Borophene heterostructure. The XPS survey spectrum (Fig. 3c) exhibits distinct peaks for Ni 2p (~855.8 eV, ~873.1 eV), O 1s (~530.13 eV), and B 1s (~188.0 eV, ~189.2 eV), thereby affirming the existence of nickel, oxygen, and boron in the composite [67,68]. The lack of supplementary peaks indicates the high purity of the synthesized NNB compound [69]. The high-resolution Ni 2p spectrum (Fig. 3d) displays two principal peaks associated with Ni $2p_3/_2$ (~855.8 eV) and Ni $2p_1/_2$ (~873.1 eV), accompanied by their corresponding satellite signals at ~861.3 eV and ~879.6 eV, thereby affirming the existence of Ni^{2+} in NiO. A minor contribution is also found at around 856.5 eV (Ni $2p_3/_2$) and 874.8 eV (Ni $2p_1/_2$), indicative of metallic Ni (Ni^0). This validates the establishment of the NiO/Ni heterojunction, which enhances charge transport

capability and interfacial charge transfer [70,71]. The B 1s spectrum (Fig. 3e) shows two distinct peaks at ~187.9 eV and ~189.2 eV, matching with B–B and B–O bonding states, respectively. The peak at ~187.9 eV represents the B–B bond, confirming the presence of pristine borophene in the composite. The signals at ~189.2 eV is ascribed to B–O bonds, indicating partial oxidation of borophene, likely due to interaction with NiO [34,72]. The O 1s spectrum (Fig. 3f) exhibits a dominant peak at ~530.1 eV, corresponding to lattice oxygen in NiO [56,73,74]. A secondary peak at ~531.5 eV is attribued to surface oxygen species (B–O, hydroxyl groups, or adsorbed oxygen). The presence of NiO-related oxygen confirms the stable integration of NiO into the NNB composite [49,64,75]. The B–O contribution suggests strong interfacial interactions between borophene and NiO [76,77].

The Nitrogen sorption isotherms and corresponding pore size distribution profiles for the NNB composites (NNB-0, NNB-20, NNB-40) and NiO are illustrated in Fig. 4. These findings elucidate the surface area, porosity, and textural characteristics of the materials. All samples show a classic type IV isotherm with a pronounced hysteresis loop, symptomatic of mesoporous materials [57,78,79]. The specific adsorption capacity rises with the borophene concentration in the composite, signifying an augmented surface area and porosity in borophene-rich samples. Among the evaluated materials, NNB-40 demonstrates the greatest nitrogen absorption, indicating a superior pore capacity and improved textural characteristics relative to NNB-0 and pure NiO. The adsorption at elevated relative pressure ($P/P_0 > 0.8$) indicates the existence of bigger mesopores or macropores. The integration of borophene nanosheets enhances porosity by creating interconnected two-dimensional channels, resulting in improved surface accessibility. The pore size distribution curve (Fig. 4b) further validates the existence of mesopores throughout the 2–50 nm range across all samples. NNB-40 has the greatest cumulative pore volume, succeeded by NNB-20 and NNB-0, thereby substantiating the augmented porosity correlated with elevated borophene content [31].

The magnetic hysteresis loops of the NNCB composites demonstrate the influence of borophene incorporation on magnetic characteristics and EMWA efficacy. The NNCB-0 sample (NiO/Ni/C without borophene) demonstrates the highest saturation magnetization (M_s = 35 emu/g) attributable to its elevated Ni content, which greatly influences magnetic loss mechanisms but may result in increased reflection losses if impedance matching is not properly tuned. With the increasing borophene content in NNCB-20 (20 % B) and NNCB-40 (40 % B), the magnetization diminishes due to the breakdown of long-range Ni/NiO magnetic ordering, with NNCB-40 exhibiting the lowest M_s (~25 emu/g). The coercivity (H_k) escalates with the increment of borophene content, with NNCB-40 demonstrating the highest H_k (~220 Oe) attributed to robust interfacial polarization and charge accumulation, which constrains domain wall movement [80].

The magnetic hysteresis loops of the NNCB composites (Fig. 4c) illustrate the influence of borophene incorporation on magnetic properties and, subsequently, electromagnetic wave attenuation (EMWA) efficacy. The NNCB-0 sample (NiO/Ni/C devoid of borophene) demonstrates the highest saturation magnetization (Ms = 35 emu/g), principally attributable to its elevated metallic Ni concentration. This robust magnetic response amplifies magnetic loss through domain wall movement and intrinsic resonance, although it may also lead to significant reflection losses if impedance matching is inadequate. As the borophene content increases in NNCB-20 (20 wt %) and NNCB-40 (40 wt %), the saturation magnetization steadily diminishes, with NNCB-40 exhibiting the lowest Ms (~25 emu/g). The decrease is ascribed to the disruption of long-range magnetic ordering among Ni/NiO particles due to the intercalation of borophene nanosheets into the structure. Concurrently, coercivity (Hc) escalates with increased borophene concentration, with NNCB-40 attaining a maximum Hc of around 220 Oe. The increase in coercivity is associated with interfacial polarization and localized charge accumulation at the borophene–Ni/NiO interfaces, which impede domain wall motion and enhance magnetic anisotropy [81]. NNCB-20 exhibits a balanced magnetic profile characterized by moderate Ms and relatively high Hc, which collectively enhance effective EM attenuation. A moderate Ms enables adequate magnetic dipole alignment while ensuring impedance matching, however a heightened Hc

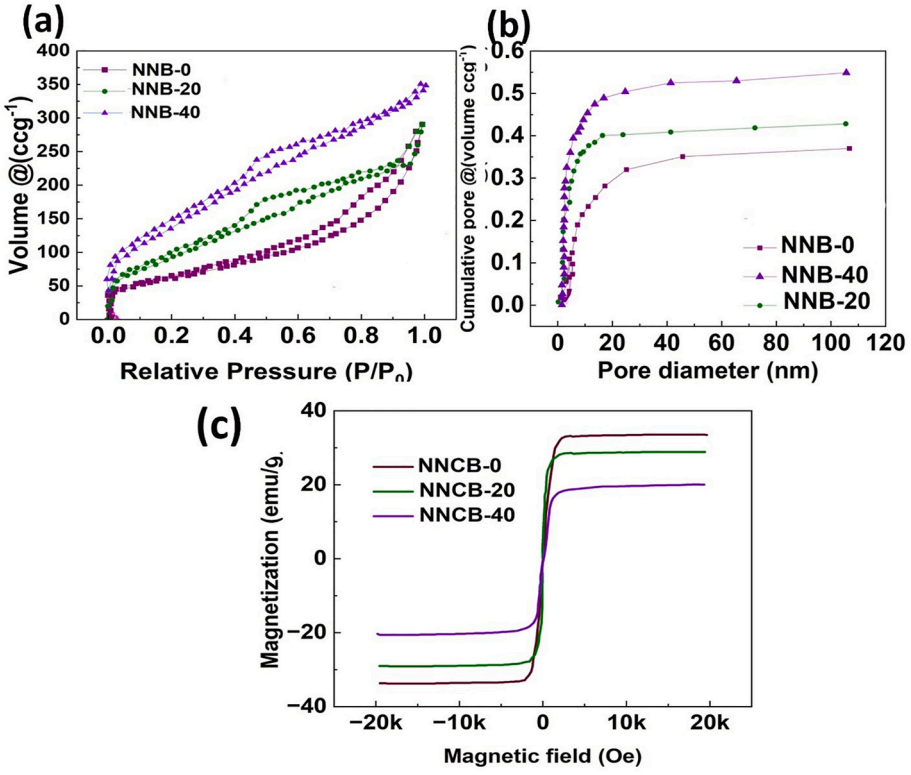

Fig. 4. (a) N_2 adsorption-desorption isotherm, (b) pore size distribution of NNB-0, NNB-20, and NNB-40 (c) magnetic hysteresis loops fabricated composites.

signifies increased energy dissipation via magnetic hysteresis and resonance mechanisms. Moreover, the embedded Ni nanoparticles create supplementary eddy current loss, especially at elevated frequencies, as a result of circulating currents generated in conductive regions. The interplay of natural resonance, magnetic hysteresis, and eddy current loss mechanisms in NNCB-20 leads to enhanced magnetic loss characteristics. The magnetic characteristics, when coupled with its exceptional dielectric performance and structural uniformity, elucidate the minimal reflection loss (RL) and the widest effective absorption bandwidth (EAB) noted in the NNCB-20 composite.

The electromagnetic properties of the NNCB-0, NNCB-20, and NNCB-40 nanocomposites were systematically analyzed to evaluate their potential for microwave absorption. The EMWA of microwave absorbing materials (MAMs) is primarily governed by their EM parameters, specifically the complex permittivity ($\varepsilon = \varepsilon' - j\varepsilon''$) and complex permeability ($\mu = \mu' - j\mu''$). Here, the real parts (ε', μ') represent the storage capability of EM energy, while the imaginary parts (ε'', μ'') correspond to energy dissipation, contributing to dielectric and magnetic losses [82, 83]. The dielectric characteristics and loss mechanisms of the NNCB composites were examined to evaluate their potential for EMWA. The obtained results are shown in Fig. 5 The trends in real permittivity (ε′) (Fig. 5a), imaginary permittivity (ε″) (Fig. 5b), permeability (μ′, μ″), dielectric loss tangent (tanδε) (Fig. 5c), and throughout the 2–18 GHz frequency range demonstrate the influence of borophene integration on charge transport, dipole relaxation, and interfacial polarization phenomena. According to Debye theory [84–86]:

$$\boldsymbol{\varepsilon}'_{\tau}(\boldsymbol{\omega}) = \varepsilon_{\infty} + \frac{(\varepsilon_s - \varepsilon_{\infty})}{(1 + j\omega\tau)} \tag{1}$$

ε_s: Static permittivity (low-frequency limit, peak polarization).

ε_∞: High-frequency permittivity (when polarization fails to synchronize with the field).

Angular frequency of the electromagnetic wave ($\omega = 2\pi f$).

τ: The relaxation time, a time constant for dipole reorientation.

Splitting into real and imaginary components:

$$\varepsilon'(\omega) = \varepsilon_{\infty} + \frac{(\varepsilon_s - \varepsilon_{\infty})\omega\tau}{1 + (\omega\tau)^2} \tag{2}$$

$$\varepsilon''(\omega) = \frac{(\varepsilon_s - \varepsilon_{\infty})\omega\tau}{1 + (\omega\tau)^2} \tag{3}$$

This produces a semicircular curve (Debye relaxation peak) when graphing ε′ against ε′′, referred to as the Cole-Cole plot. The peak's breadth and position are contingent upon τ, indicating the material's relaxation dynamics. Furthermore, conductive loss contributes to ε′′, represented as [87–89]:

$$\varepsilon''_{cond} = \frac{\sigma_{ac}}{\omega f \varepsilon_0} \tag{4}$$

where σ is the electrical conductivity and ε_0 is the permittivity of open space (8.85×10^{-12} F/m). The total ε′′ comprises the aggregation of relaxation and conductive losses.

The real and imaginary components signify a material's capacity for storing and dissipating electromagnetic energy, while their ratio indicates the dielectric loss tangent

$$\tan\delta_{\varepsilon} = \boldsymbol{\varepsilon}''/\boldsymbol{\varepsilon}' \text{ and the magnetic loss tangent } tan\ \delta_{\mu} = \boldsymbol{\mu}''/\boldsymbol{\mu}' \tag{5}$$

[90, 91].

As seen in Fig. 5a, the real permittivity (ε′) of NNCB-20 is lower than that of NNCB-0 and NNCB-40, indicating a reduction in excessive conductivity losses, hence preventing unnecessary reflection of incident electromagnetic waves. In Fig. 5b, the imaginary permittivity (ε″) of NNCB-20 is inferior to that of NNCB-0 but superior to NNCB-40, signifying an ideal equilibrium between energy storage and dielectric loss. NNCB-40 exhibits a markedly reduced ε″, potentially resulting in inadequate microwave attenuation. Fig. 5c shows the dielectric loss tangent (tanδε), where NNCB-20 exhibits a moderate loss factor compared to

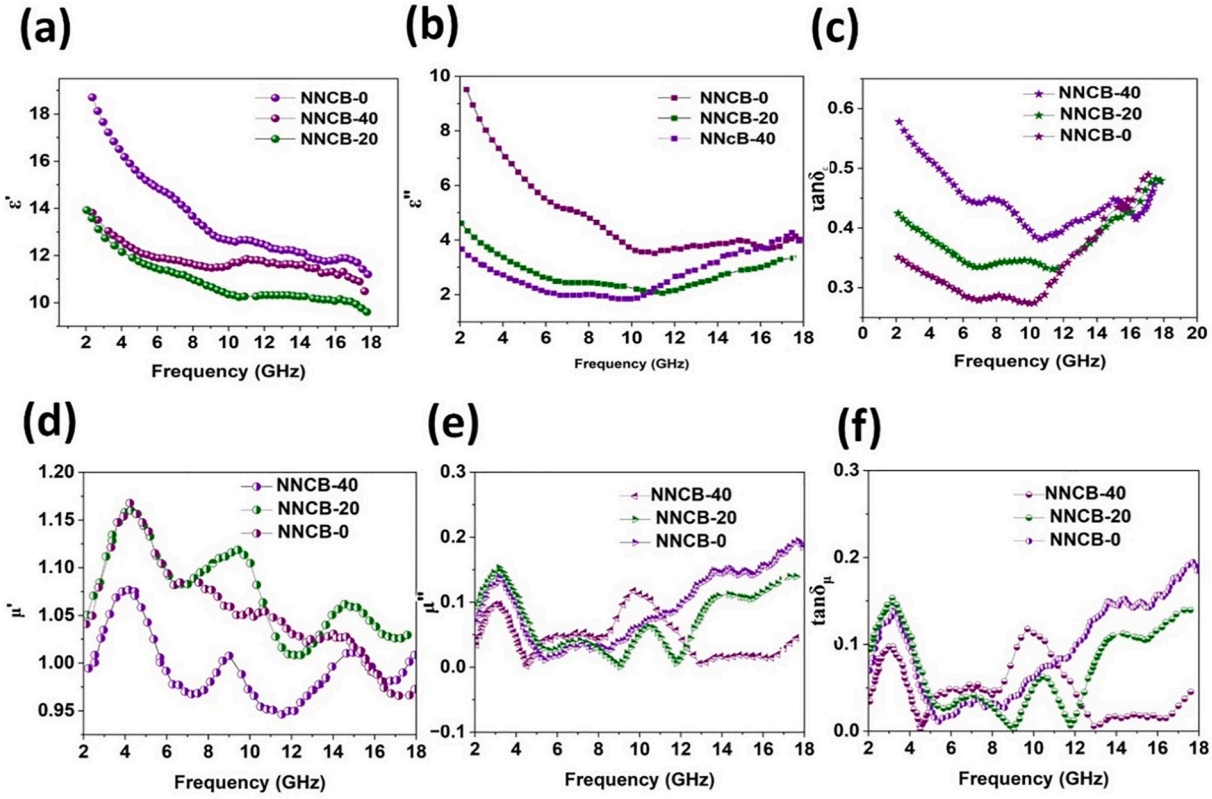

Fig. 5. Electromagnetic characteristic of the NNCB-40,NNCB-20, NNCB-0 (a) ε′, (b) ε″, (c) tan δ_ε (d) μ′, (e) μ′, (f) *tan* δ_μ

NNCB-0 and NNCB-40. NNCB-40 has a lower dielectric loss tangent, meaning it may not be as efficient in converting electromagnetic energy into heat. NNCB-0, on the other hand, shows excessive dielectric loss, which can lead to impedance mismatch and unwanted wave reflection instead of absorption. In Fig. 5d, the real permeability (μ') of NNCB-20 is marginally superior to that of NNCB-40, signifying enhanced magnetic energy storage capabilities. Fig. 5e demonstrates that the imaginary permeability (μ'') of NNCB-20 exhibits greater stability than that of NNCB-40, indicating that NNCB-20 maintains effective magnetic loss processes, such as natural resonance and eddy current effects. The presence of dielectric and magnetic loss guarantees that NNCB-20 attains enhanced attenuation of incident electromagnetic waves. Fig. 5f shows that the magnetic loss tangent ($\tan\delta\mu$) for NNCB-20 is more optimized compared to NNCB-40, where the fluctuations in NNCB-40 suggest an unstable loss mechanism. The presence of dielectric and magnetic loss guarantees that NNCB-20 attains enhanced attenuation of incident electromagnetic waves.

Reflection Loss (RL), the frequency range in which the return loss (RL) falls below a certain threshold (often −10 dB), indicating that a minimum of 90 % of incoming electromagnetic waves are absorbed, and effective absorption bandwidth (EAB), measures the amount of electromagnetic wave energy reflected from the surface of an absorber, are critical metrics for assessing the microwave absorption characteristics of materials. Transmission Line Theory is extensively employed to evaluate the microwave absorption characteristics of materials. The effectiveness of an absorber depends on its ability to minimize reflection and maximize energy dissipation through dielectric and magnetic losses. Efficient absorption occurs when the input impedance of the material (Z_{in}) is close to the characteristic impedance of free space ($Z_0 = 377\Omega$).

Utilizing the transmission line model, one can identify the interaction of an absorbing material with incident microwaves and appropriately design impedance-matched materials for improved absorption.

$$Z_{in} = Z_0 \tan h\left(j\frac{2\pi f}{c} d\sqrt{\mu_r \varepsilon_r}\right) \quad (6)$$

Where Z_{in} is the input impedance of the absorbing material, Z_0 is the characteristic impedance of free space (377 Ω), f = Frequency of the incident wave (GHz), C= Speed of light in vacuum (3.0×10^8 m/s), d = Thickness of the absorber (mm), μ_r = Relative permeability of the material, ε_r = relative permittivity of the material.

$$RL = 20\log_{10}|\Gamma| \quad (7)$$

where Γ is the reflection coefficient.

$$\Gamma = \frac{Z_{in} - Z_0}{Z_{in} + Z_0} \quad (8)$$

When the RL was below −10 dB, almost 91 % of electromagnetic waves were effectively attenuated, and the associated frequency band is designated as the EAB.

Fig. 6(a–f) illustrate the RL characteristics of the NNCB-0, NNCB-20, and NNCB-40 nanocomposites across a broad frequency range (2–18 GHz) and varying thicknesses. These results are critical for evaluating the EMA capability of each composition and determining the optimal material for practical applications such as EMI shielding and stealth technology. As seen in Fig. 6a, RL_{min} reaches −25.1 dB at 16.8 GHz with a thickness of 1.6 mm. This composition exhibits significant absorption in the Ku-band, although its overall absorption intensity is inferior to that of NNCB-20. The corresponding 3D RL surface plot (Fig. 6d) demonstrates that NNCB-40 displays comparatively inferior absorption characteristics, with the RL minimum attaining merely −25.1 dB, signifying inadequate attenuation of electromagnetic waves. The NNCB-20, (Fig. 6b), demonstrates the highest absorption efficacy, attaining RL_{min} = −55.5 dB at 12.8 GHz with an optimum thickness of 1.97 mm. The absorption bandwidth, with RL below −10 dB, is wider, encompassing several frequency ranges, so affirming that NNCB-20 offers optimal impedance matching and attenuation. 3D reflection loss analysis shows the deepest absorption valley is observed for NNCB-20. The broader absorption region confirms its superior microwave absorption efficiency, making it the optimal composition for EMI shielding. The minimum RL is −48.5 dB at 11.8 GHz, achieved with a thickness of 2 mm. Though it shows significant absorption, the absorption intensity and effective bandwidth are slightly inferior to NNCB-20. While NNCB-0). Fig. 6c and f demonstrates significant absorption at −48.5 dB, its absorption bandwidth and peak performance are slightly lower than NNCB-20, indicating that 20 wt % borophene content offers the best balance between dielectric and magnetic losses. The enhanced performance results from the combination of various electromagnetic loss

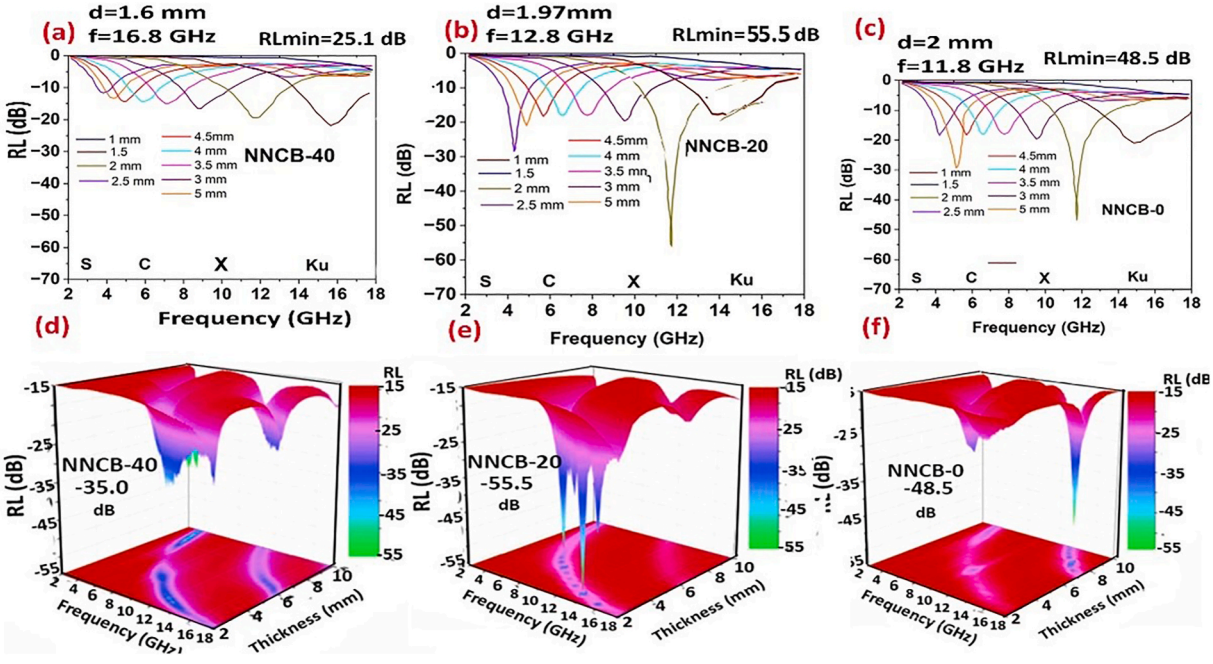

Fig. 6. RL and 3D RL mappings of (a,d) NNCB-40; (b,e) NNCB-20; (c,f) NNCB-0.

processes inside the hierarchical NiO/Ni/Borophene composite. Dielectric loss, resulting from dipole and interfacial polarization, is amplified by the heterogeneous interfaces among NiO, Ni, carbon foam, and borophene nanosheets. These interfacial areas function as polarization centers that capture and discharge electromagnetic energy via relaxation processes. Furthermore, the conductive network established by nickel and borophene induces conduction loss, as alternating current produces Joule heating through charge transport channels. This mechanism is notably evident in NNCB-20, where the conductive filler content is tuned to sustain impedance matching without causing excessive reflection, in accordance with the findings reported by Wu et al. [90] and Feng et al. [91]. Simultaneously, magnetic loss mechanisms are initiated by the presence of Ni nanoparticles, which display soft ferromagnetism. These losses result from natural resonance, hysteresis loss, and eddy current phenomena. The amalgamation of Ni and NiO induces various magnetic relaxation processes, whilst the mild saturation magnetization (Ms) of NNCB-20 facilitates impedance compatibility. This aligns with the magnetic attenuation contributions outlined in Ref. [92] where Ni-based composites exhibited multi-resonance behavior attributable to multiple magnetic phases.

Moreover, the RL peak shifted to lower frequencies as the sample thickness increased; this phenomenon can be accounted for using the quarter-wavelength matching model as follows [7,93]:

$$d = \frac{\lambda}{4} = \frac{c}{4f\sqrt{\mu_r \varepsilon_r}} \tag{9}$$

d = thickness of the absorber (mm), λ = wavelength of the electromagnetic wave in the absorber, c = light velocity in vacuum (3.0×10^8 m/s), f = resonant frequency of absorption (GHz), μ_r = relative permeability of the absorber, ε_r = relative permittivity of the absorber. Meeting the criteria outlined in fulfilled Eq. (3), the phase shift between the received and reflective electromagnetic waves was 180°, resulting in complete cancellation of the reflected waves at the interface between the absorber and air, thereby attaining the minimal reflection loss value. The measured thickness values corresponded well with the simulation results depicted in Fig. 7a–c, demonstrating that the material complied to the model. Targeted impedance synchronization (Z) is essential for obtaining effective microwave absorption. Optimal impedance matching takes place when the input electromagnetic wave is entirely absorbed by the material with Z = 1. NNCB-40 exhibited Z values under 0.9 (Fig. 7d), signifying inadequate impedance matching. The Z value of the NNCB-20, NNCB-0 composite significantly surpassed that of CCS, showing that the higher concentration of the magnetically active substance reduced the impedance mismatch (Fig. 7e). The Z value of the NNCB-20 composite varied around 1 across a far broader spectrum of frequencies and thicknesses (Fig. 7f), indicating optimal impedance matching.

Another key parameter that quantifies the ability of a material to absorb and dissipate electromagnetic waves is the attenuation coefficient (α) It delineates the attenuation of an electromagnetic wave's amplitude as it traverses a medium, attributable to energy dissipation mechanisms like dielectric loss, magnetic loss, and scattering [100,101].

$$\alpha = \frac{\sqrt{2}}{c}\pi f\left[\mu''\varepsilon''\left(\sqrt{1+\frac{\tan\delta_e \tan\delta_m}{\mu'\varepsilon'}}-1\right)\right]^{1/2} \tag{10}$$

f = frequency of the electromagnetic wave (Hz), c = speed of light in vacuum (3.0×10^8), μ real part of the relative permeability (magnetic

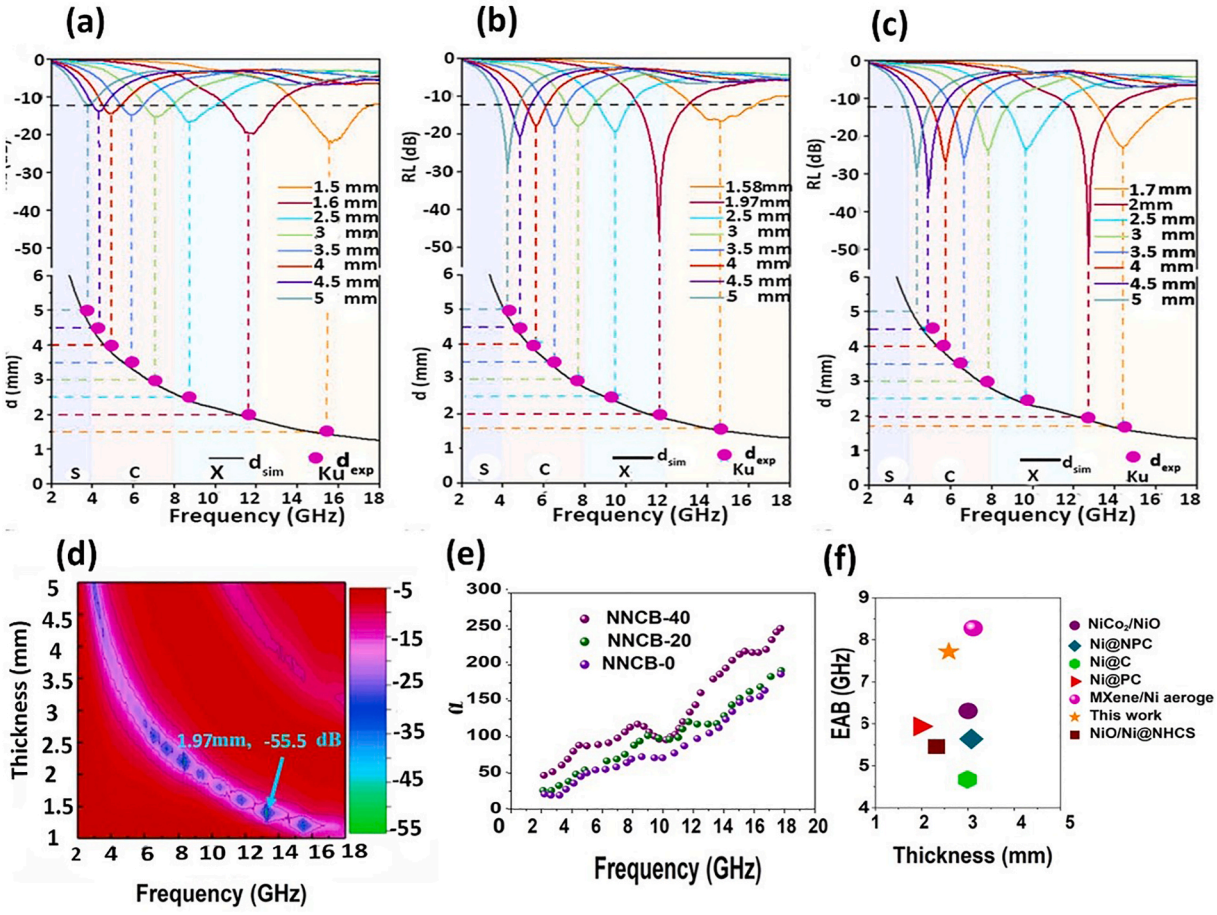

Fig. 7. Quarter-wave matching layer approach (a)NNCB-40, (b) NNCB-20, (c) NNCB-0 (d) 2D contour data representing Z values of NNCB-20, (e) attenuation coefficients of the composites, (f) comparison of effective absorption bandwidth and related width among various absorbing materials [94–99].

property), ϵ' = real part of the relative permittivity (dielectric property), $tan\,\delta_e = \varepsilon''/\varepsilon'$ (dielectric loss tangent), $tan\,\delta_m = \mu''/\mu'$ (magnetic loss tangent).

The α-values of NNCB-0, NNCB-20, and NNCB-40 composites exhibited a rise with frequency (Fig. 7e). NNCB-40 demonstrated the highest α-value owing to its greater conductive loss; yet, it showed inefficient microwave absorption capability because to a disparity between dielectric and magnetic losses. The NNCB-20 composite demonstrated a superior attenuation coefficient compared to the NNCB-0composite, consistent with the RL findings. While NNCB-40 shows the highest α, it suffers from poor impedance matching, leading to reflection at the interface. NNCB-0 lacks sufficient dielectric polarization centers, limiting its absorption capability despite acceptable matching. Only NNCB-20 strikes a balance between attenuation strength and wave penetration depth, achieving a Z value approaching 1 across a broad frequency range—an essential criterion for ideal absorbers, as emphasized in Ref. [102]. Thus, tuned impedance matching, ensuring maximum energy dissipation and minimal reflection.

The comparison of the NNCB-20 composites, which exhibits the broadest effective absorption bandwidth (EAB) and optimal thickness against other Nickel-derived microwave absorbing materials (Fig. 7f), substantiates its superior microwave absorption efficacy.

Mechanisms of dielectric energy dissipation employing Cole-Cole plots Fig. 8a-c according to the Debye relaxation theory, as outlined: The Cole-Cole plots depicts the polarization relaxation process as a semicircle [32]. The semicircle width indicating relaxation strength polarization loss. Dipolar polarization loss occurs due to the realignment of dipoles in response to an alternating electromagnetic field [27,80].

$$\varepsilon' = \varepsilon_\infty + \frac{(\varepsilon_s - \varepsilon_\infty)}{1 + (\omega\tau)^2} \tag{11}$$

$$\varepsilon'' = \frac{(\varepsilon_s - \varepsilon_\infty)}{1 + (\omega\tau)^2} \tag{12}$$

ϵ_s is the static permittivity (low-frequency limit), ϵ_∞ = is the high-frequency permittivity (at infinite frequency), $\omega = 2\pi f$ is the angular frequency, τ is the relaxation time (time taken for dipoles to reorient).

The presence of defects, vacancies, and heterostructures (NiO/Ni interfaces and borophene layers) enhances dipolar relaxation, particularly in the NNCB-20 sample. Furthermore, the conductive loss can be seen as a straight line. As seen in Fig. 8. The number of semicircles is directly correlated with the Ni concentration. This is evident in Fig. 8c, which reveals a higher number of relaxation processes in the NNCB-0 composite. As depicted in the Cole-Cole plot in Fig. 8c, the NNCB-0 composite exhibits an arc with increased curvature, representing enhanced dielectric polarization loss primarily attributed to the interface-induced phenomena between the NiO and Ni phases. The enhanced slope of the extended linear tail line in NNCB-20 and NNCB-40 relative to the NNCB-0 composite may be ascribed to the incorporation of the B/NiO/Ni heterostructure, which altered the arrangement of electrons and improved electrical conductivity, supporting the findings from the analysis of the ε" value variation with incidence and XPS studies' findings.

Magnetic losses in microwave-absorbing materials are mostly due to phenomena including natural resonance, exchange resonance, domain wall resonance, and eddy current loss [85,103]. Eddy current loss significantly impacts conductive and magnetic materials, especially at elevated frequencies. Eddy currents are circulating electrical currents generated in a conductor subjected to a time-varying magnetic field. These currents generate a counteracting magnetic field, resulting in energy loss by Joule heating. The eddy current loss coefficient (C_0) evaluates whether the magnetic loss in a material is predominantly attributable to eddy currents or alternative causes, such as intrinsic magnetic resonance or domain wall motion.

The coefficient of eddy current loss is expressed as [104]:

$$C_0 = \frac{\mu''(f)}{(\mu'(f))^2 . f} = \frac{2}{3}\pi\mu_0 D^2\sigma \tag{13}$$

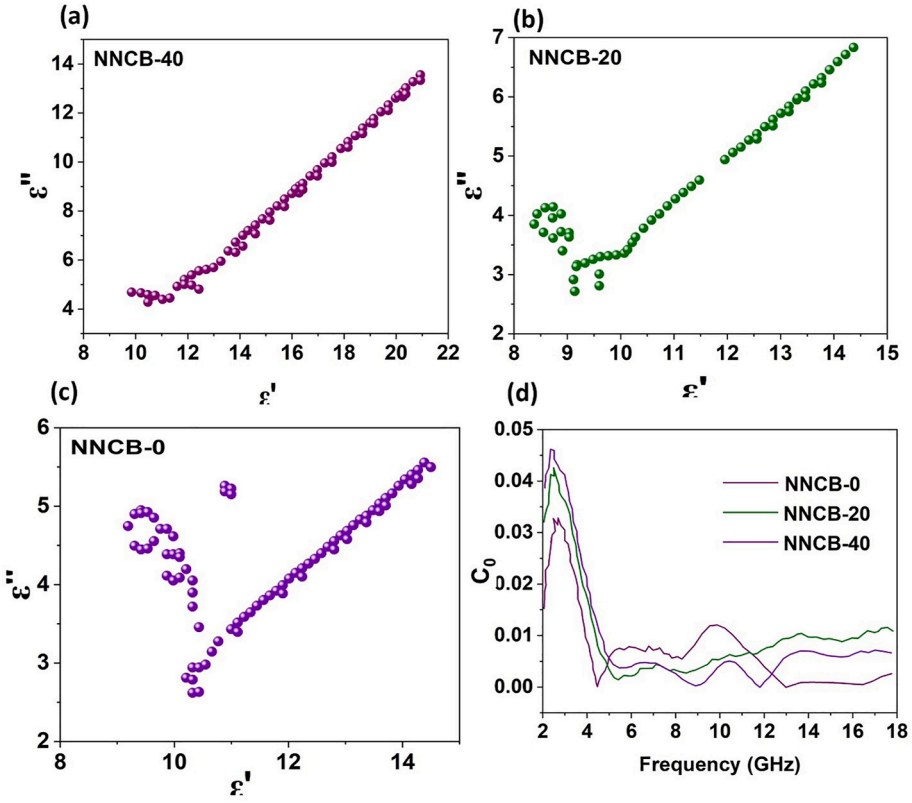

Fig. 8. Cole–Cole plots of (a) NNCB-40, (b)NNCB-20, (c)NNCB-0; (d) frequency dependence C_0 of fabricated composites.

Where μ'' = imaginary part of permeability (magnetic loss component), μ = real part of permeability (magnetic storage component), f = frequency (GHz), *D* is the particle size of magnetic grains.

Fig. 8d illustrates that the C_0 curves of all samples exhibited fluctuations between 2 and 14 GHz, demonstrating that magnetically induced energy loss primarily stemmed from intrinsic magnetic resonance within that frequency range. As the frequency grew, C_0 remained rather constant, suggesting that eddy current losses at elevated frequencies contributed to the magnetism-related dissipation phenomena.

The radar cross-section (RCS) measures the magnitude of the backscattered echoes a target when exposed to radar waves, indicating the object's detectability by radar [82]. An increased RCS indicates that the entity is more detectable by radar systems. The cross-sectional radar signature is affected by the target's geometry, dimensions, composition, and material properties, in addition to spectral, polarization, and directional properties of the incoming EM radiation [105]. To evaluate potential uses of NNCB-20 composites in electromagnetic wave absorption, we conducted radar cross-section simulations utilizing Computer Simulation Technology (CST) software. The actual in-situ electromagnetic wave absorption properties were assessed for NNCB-0, NNCB-20, NNCB-40 on 100 × 100 mm^2 coated plates, as seen in Fig. 9a–d. The angle at which the EM wave strikes the surface varies from −60° to 60° at an applied frequency of 6 GHz. Fig. 9a depicts the three-dimensional radar wave scattering map of the perfectly electrically conductive surface devoid of any absorber covering. In Fig. 9b–d, there is almost no dispersed electromagnetic wave seen at the incident backside of the coated plate, signifying near-total attenuation of the incoming wave. Fig. 9 e illustrates that the disparity in RCS values between the PEC and NNCB-20 is 29.95 dB m^2. The superior RCS suppression capability of NNCB-20 underscores its significant promise for practical applications.

The potential electromagnetic wave absorption mechanism of NNGA composites is depicted in Fig. 10. Initially, the flower-like NiO/Ni integrated into the 3D B forms an organized porous framework, facilitating an improved transmission pathway for electromagnetic waves, hence enhancing multiple reflection and scattering [104]. Due to superior impedance matching, the electromagnetic waves can rapidly penetrate the heterostructures with minimal reflection, facilitating effective absorption. Secondly, the conducting pathways can generate increased microampere currents when an external electric field is applied to NNCB [106]. The presence of defects on borophene nanosheets results in defects and curvature, which facilitate defect-driven polarization decay and enhance electron transport velocity. The presence of a heterogeneous junction among NiO, Ni, and B could improve interfacial polarization. Moreover, a dynamic magnetic field will generate currents, resulting in the conversion of electromagnetic waves into thermal energy. Lastly, the NiO/Ni incorporated into B can induce magnetic loss due to various causes, resulting in improved impedance matching.

Currently, enhanced stability is essential to ensure long-term efficacy in realistic service conditions. The NNCB-20 composites magnetic absorber will interact with corrosive agents, such as oxygen and acidic solutions, leading to corrosion and degradation of absorption properties, which hinders practical implementation. Fig. 11 systematically illustrates the chemical resilience and enduring electromagnetic (EM) absorption efficacy of the NNB-20 nanocomposite during extended exposure to a corrosive acidic milieu, specifically 1 M HCl. The collection of photos and graphs provided provide a thorough assessment from macroscopic integrity to functional performance preservationFig.11a displays an image of the NNB-20 nanocomposite submerged in 1 M HCl for a duration of 24 h. The nanocomposite stays clearly intact, exhibiting no substantial evidence of breakdown, dispersion, or precipitation. The unique black layer indicates that the material preserves structural integrity despite the harsh acidic environment. This observation indicates robust chemical bonding and acid-resistant interfaces among the components of NiO, Ni, and borophene. Notably, borophene, despite being a two-dimensional material, appears to gain from hybrid stabilization with metal or metal oxide phases, which mitigates oxidative or proton-induced deteriorate. Fig. 11b displays an image of the water contact angle for the NNB-20 sample following acid exposure. The elevated contact angle verifies the maintenance of hydrophobicity on the composite surface. This indicates that the surface functional groups and morphology are mainly unchanged by HCl treatment, which is essential for practical applications where material wettability is linked to corrosion resistance, durability, and performance reliability. Hydrophobic surfaces can reduce water absorption and postpone degradation processes, hence improving the material's durability in humid or chemically hostile settings. Fig. 11c presents a 3D reflection loss plot of the acid-treated NNB-20 throughout an extensive frequency range of 2–18 GHz and a thickness range of 1–5 mm. The measurements indicate a significant minimum reflection loss value of −50.5 dB at 13.7 GHz with a thickness of 1.2 mm, exemplifying highly efficient microwave

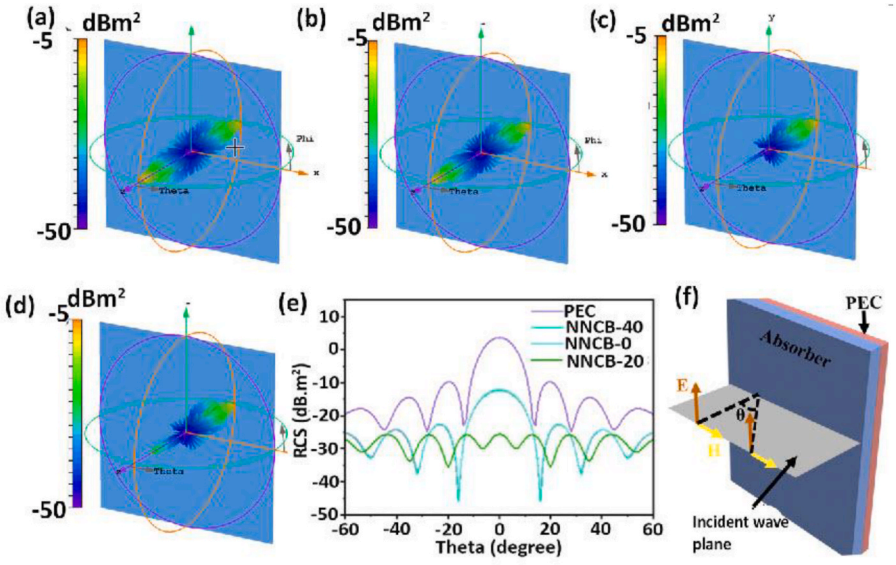

Fig. 9. 3D Radar Cross Section (RCS) simulations: for a rectangular perfect electrical conductor (PEC),(a) without coating, with an absorber coating (b) NNCB-0, (c) NNCB-20, (d) NNCB-40 and (e) RCS simulations of NNCB-0, NNCB-20, NNCB-40 at different scanning angles (f) rectangular PEC covered with an absorber coating.

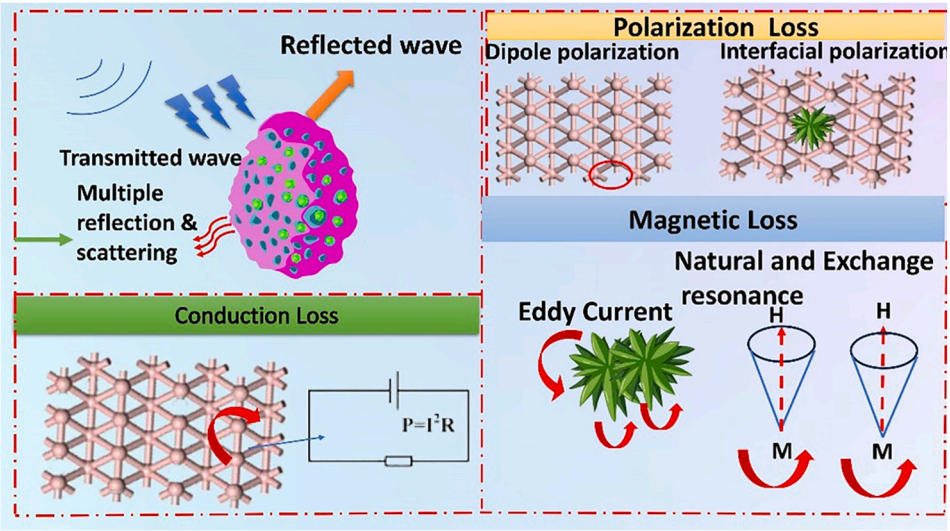

Fig. 10. Multifaceted synergistic energy dissipation within the NNCB absorbers.

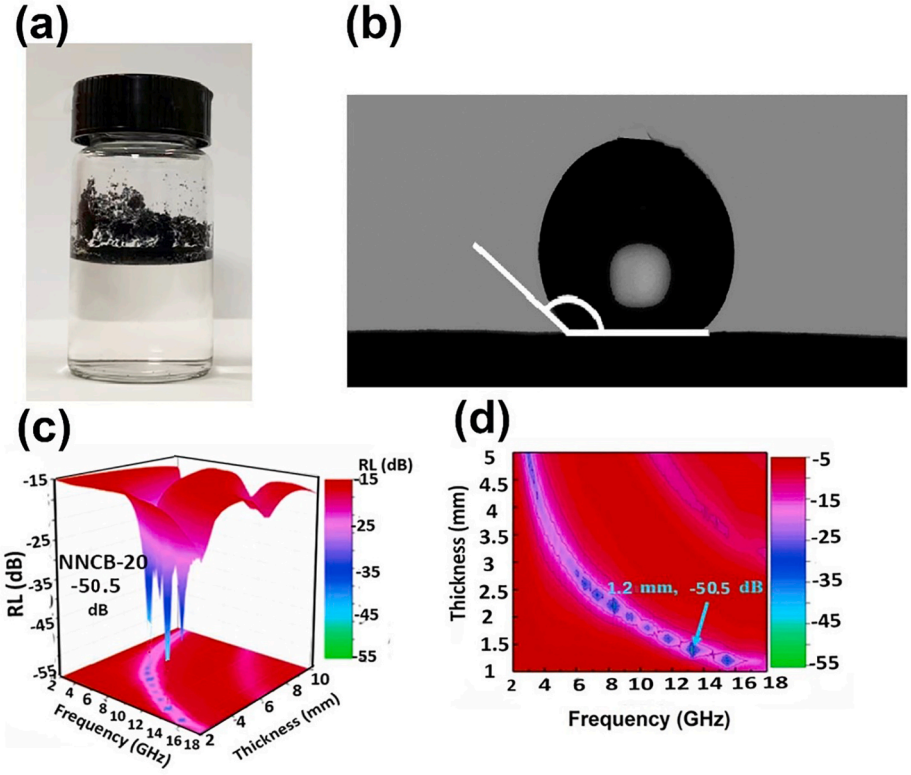

Fig. 11. (a) Photograph of the NNB-20 nanocomposite after 24 h of soaking in 1 M HCl, (b) Water contact angle measurement of NNB-20 post-HCl treatment, (c) 3D, and (d) 2D reflection loss (RL) plot of NNB-20 after acid exposure.

absorption. This performance metric is either identical to or significantly enhanced compared to the untreated NNB-20 (as indicated in baseline investigations), suggesting that the acidic environment has not undermined the microwave attenuation properties of the material. Fig. 11d confirms the observation via a 2D contour map, emphasizing the frequency-thickness domain where maximal absorption transpires. The blue contour line at −50.5 dB and 1.2 mm is distinctly delineated, signifying a pronounced and narrowband absorption peak. This indicates that the material maintains its absorption capacity while demonstrating negligible widening or frequency response shifts, which may otherwise signify partial degradation or modified permittivity/permeability profiles resulting from acid exposure.

4. Conclusion

A novel 3D hierarchical NiO/Ni/Borophene (NNCB) nanocomposite was successfully synthesized using a scalable, solution-based approach that combines solvothermal synthesis, liquid-phase exfoliation, and freeze-drying processes. The integration of borophene into the NiO/Ni framework mitigates the intrinsic drawbacks of conventional composites—namely high density, impedance mismatch, and restricted dielectric loss—by providing lightweight conductivity, anisotropic charge

transport, and improved interfacial polarization. The NNCB-20 composition exhibited the most advantageous electromagnetic wave absorption characteristics among the synthesized materials, attaining a minimal reflection loss of −55.5 dB and a wide effective absorption bandwidth due to its balanced dielectric and magnetic losses. Structural investigations validated the homogeneous distribution of NiO/Ni nanoparticles on borophene nanosheets, whereas surface and magnetic characterizations disclosed synergistic mechanisms encompassing conduction loss, dipole polarization, interfacial contact, and multiple scattering. This study demonstrates borophene's capability as a multifunctional additive in electromagnetic absorbing materials and provides a design framework for advanced, lightweight, and high-efficiency EMI shielding materials applicable in communications, aerospace, and stealth technologies.

CRediT authorship contribution statement

Wala Dizayee: Writing – original draft, Software, Project administration, Methodology, Formal analysis, Data curation, Conceptualization. **Mohammed Ahmed Mohammed:** Writing – original draft, Visualization, Validation, Supervision, Resources, Project administration, Methodology, Funding acquisition, Conceptualization. **Mohammed Zorah:** Supervision, Resources, Project administration, Methodology, Investigation, Formal analysis, Data curation, Conceptualization. **HassabAlla M.A. Mahmoud:** Conceptualization, Data curation, Project administration, Resources, Validation, Visualization, Writing – review & editing. **Mohamed Shabbir Abdulnabi:** Supervision, Software, Resources, Project administration, Investigation, Funding acquisition, Data curation. **G. Abdulkareem-Alsultan:** Writing – review & editing, Writing – original draft, Visualization, Validation, Supervision, Software, Resources, Project administration, Methodology, Investigation, Funding acquisition, Formal analysis, Data curation, Conceptualization. **Maadh Fawzi Nassar:** Writing – review & editing, Writing – original draft, Visualization, Validation, Supervision, Software, Resources, Project administration, Methodology, Investigation, Funding acquisition, Formal analysis, Data curation, Conceptualization.

Declaration of competing interest

The authors declare that they have no known competing financial interests or personal relationships that could have appeared to influence the work reported in this paper.

Acknowledgments

The authors extend their appreciation to the Deanship of Research and Graduate Studies at King Khalid University for funding this work through Large Research Project under grant number RGP2/155/46.

Appendix ASupplementary data

Supplementary data to this article can be found online at https://doi.org/10.1016/j.jsamd.2025.100934.

References

[1] Q. Han, et al., Structural and hetero-interfacial engineering of magnetic bimetallic composites based polyurethane microwave absorbing coating for marine environment, Compos. Appl. Sci. Manuf. (2025) 192.
[2] M.R. Tariq, et al., A comprehensive review of the advancement of transition metal oxide nanocomposites for microwave absorption, Coord. Chem. Rev. 533 (2025).
[3] N. Gao, et al., Broadband multi-unit composite metamaterial for simultaneous sound wave and electromagnetic wave absorption, Mater. Des. 251 (2025) 113671.
[4] Z. Ren, et al., Ultra-broadband perfect absorbers based on biomimetic metamaterials with dual coupling gradient resonators, Adv. Mater. 37 (11) (2025) 2416314.
[5] M.Q. Wang, M.S. Cao, Perspectives on metal-organic framework-derived microwave absorption materials, J. Mater. Sci. Technol. 214 (2025) 37–52.
[6] Y. Xu, et al., Optimized electromagnetic wave absorption properties of Ag/Fe3O4/SBA-15, Colloids Surf. A Physicochem. Eng. Asp. (2025) 711.
[7] S.S. Khatami, et al., Energy-efficient and secure double RIS-aided wireless sensor networks: a QoS-aware fuzzy deep reinforcement learning approach, J. Sens. Actuator Netw. 14 (1) (2025) 18.
[8] J. Deng, N. Gao, X. Chen, Ultrawide attenuation bands in gradient metabeams with acoustic black hole pillars, Thin-Walled Struct. 184 (2023) 110459.
[9] Y. Guan, et al., Regulable crack patterns for the fabrication of high-performance transparent EMI shielding windows, iScience 28 (1) (2025) 111543.
[10] Niu, S., et al., Breaking the trade-off between complexity and absorbing performance in metamaterials through intelligent design. Small. **n/a**(n/a): p. 2502828.
[11] C. Zhang, et al., Mechanism for the formation of natural fractures and their effects on shale oil accumulation in Junggar Basin, NW China, Int. J. Coal Geol. 254 (2022) 103973.
[12] X. He, et al., Influencing factors and quantitative prediction of gas content of deep marine shale in Luzhou block, Sci. Rep. 15 (1) (2025) 1896.
[13] Y. Zhu, et al., A robust hierarchical MXene nanocomposite by valid magnetoelectric coordination for efficient electromagnetic response, Materials Today Nano 29 (2025).
[14] M. Yi, et al., Tunable 1D-2D carbon nanomaterials for broadband and high-performance microwave absorption via ultrasonic spray ice template, ACS Appl. Mater. Interfaces 17 (6) (2025) 9702–9715.
[15] J. Xu, et al., Constructing MXene-based mixed-dimensional structure with multiple interfaces to optimize dielectric-magnetic synergistic effect for effective electromagnetic wave absorption, J. Colloid Interface Sci. 677 (2025) 529–539.
[16] W. Wang, et al., Recent progress and prospect of MXene-based microwave absorbing materials, Mater. Res. Bull. 179 (2024).
[17] M. Sathish Kumar, et al., Engineering multifunctionality graphene-based nanocomposites with epoxy-silane functionalized cardanol for next-generation microwave absorber, J. Colloid Interface Sci. 678 (2025) 407–420.
[18] J. Li, et al., MoS2-Based nanocomposites for microwave absorption: a review, ACS Appl. Nano Mater. 7 (6) (2024) 5761–5775.
[19] Z. Hashemi, A. Ramezani, M.P. Moghaddam, Energy hub management by using decentralized robust model predictive control, in: 2016 4th International Conference on Control, Instrumentation, and Automation (ICCIA), IEEE, 2016.
[20] A. Hajrasouliha, B. Shahgholi Ghahfarokhi, Dynamic geo-based resource selection in LTE-V2V communications using vehicle trajectory prediction, Comput. Commun. 177 (2021) 239–254.
[21] N. Gao, et al., Experimental verification of ultra-broadband vibration reduction of underwater vehicle pressure-resisting shells using acoustic black holes, Thin-Walled Struct. 211 (2025) 113118.
[22] Wang, X., et al., Ultra-bandwidth microwave absorption and low angle sensitivity in dual-network aerogels with dual-scale pores. Small. **n/a**(n/a): p. 2412744.
[23] C. Zhang, et al., Major factors controlling fracture development in the Middle Permian Lucaogou Formation tight oil reservoir, Junggar Basin, NW China, J. Asian Earth Sci. 146 (2017) 279–295.
[24] C. Zhang, et al., Mechanisms of bedding fracturing in the Junggar Basin, northwest China. Constraints from in Situ U-Pb Dating and CO-Nd Isotopic Analysis of Calcite Cements, Geological Society of America Bulletin, 2025.
[25] B. Zhao, et al., A novel sponge-like 2D Ni/derivative heterostructure to strengthen microwave absorption performance, Phys. Chem. Chem. Phys. 20 (45) (2018) 28623–28633.
[26] H. Wang, et al., Biomass carbon derived from pine nut shells decorated with NiO nanoflakes for enhanced microwave absorption properties, RSC Adv. 9 (16) (2019) 9126–9135.
[27] L. Huang, et al., Enhanced electromagnetic absorbing performance of MOF-derived Ni/NiO/Cu@C composites, Compos. B Eng. 164 (2019) 583–589.
[28] A.F. Ahmad, et al., Synthesis and characterisation of nickel oxide reinforced with polycaprolactone composite for dielectric applications by controlling nickel oxide as a filler, Results Phys. 11 (2018) 427–435.
[29] M. Zarei, et al., The application of multi-criteria decision analysis in gaining a premier sort of stability in airplane safety, in: Safety and Reliability, Taylor & Francis, 2024.
[30] Y. Wang, et al., SBSM-Pro: support bio-sequence machine for proteins, Sci. China Inf. Sci. 67 (11) (2024) 212106.
[31] F. Zhang, et al., Tunable electromagnetic properties of Ti 3 C 2 T x/rGO foams decorated with NiO particles, CrystEngComm 24 (33) (2022) 5949–5957.
[32] R.A. Lashaki, et al., Dendrite neural network scheme for estimating output power and efficiency for a class of solar free-piston Stirling engine, Int. J. Model. Simulat. (2025) 1–12.
[33] M. Liu, et al., Hierarchical non-singular terminal sliding mode control for constrained under-actuated nonlinear systems against sensor faults, Nonlinear Dyn. (2025) 1–17.
[34] Y. Gao, et al., Multi-phase heterostructures of flower-like Ni (NiO) decorated on two-dimensional Ti3C2Tx/TiO2 for high-performance microwave absorption properties, Ceram. Int. 47 (8) (2021) 10764–10772.
[35] M. Aali, et al., Introducing a novel temperature measurement to analyze the effect of hybrid cooling methods on improving solar panel performance: an experimental approach, Appl. Therm. Eng. (2025) 125889.
[36] C. Zhang, et al., Formational stages of natural fractures revealed by U-Pb dating and C-O-Sr-Nd isotopes of dolomites in the Ediacaran Dengying Formation, Sichuan Basin, southwest China, GSA Bulletin 136 (11–12) (2024) 4671–4688.

[37] C. Zhang, et al., Magmatism and hydrocarbon accumulation in sedimentary basins: a review, Earth Sci. Rev. 244 (2023) 104531.
[38] A. Pandey, et al., Power dependent tunable optical nonlinearity in Iron oxide/Borophene core-shell nanoparticles under ultrashort laser excitation, Opt Laser. Technol. 181 (2025) 111761.
[39] Z. Wang, et al., Permanent magnet-based superficial flow velometer with ultralow output drift, IEEE Trans. Instrum. Meas. 72 (2023) 1–12.
[40] J. Cai, et al., Adaptive backstepping control for a class of nonlinear systems with output modeling error and external disturbance, Trans. Inst. Meas. Control (2025) 01423312251318793.
[41] F. Wei, et al., Dynamic memory event-triggered adaptive neural prescribed-time bipartite consensus control for high-order MASs with privacy preservation, Commun. Nonlinear Sci. Numer. Simulat. 145 (2025) 108693.
[42] N. Fayzullaev, et al., Enhancing Li-S battery performance by harnessing the power of single atoms on 2D borophene, Electrochim. Acta (2025) 145831.
[43] P. Das, et al., Borophene based 3D extrusion printed nanocomposite hydrogel for antibacterial and controlled release application, Adv. Funct. Mater. (2024) 2314520.
[44] P. Kumar, et al., The rise of borophene, Prog. Mater. Sci. (2024) 101331.
[45] H. Lin, et al., Scalable production of freestanding few-layer β12-borophene single crystalline sheets as efficient electrocatalysts for lithium–sulfur batteries, ACS Nano 15 (11) (2021) 17327–17336.
[46] M. Faraji, et al., Two-dimensional materials in semiconductor photoelectrocatalytic systems for water splitting, Energy Environ. Sci. 12 (1) (2019) 59–95.
[47] G.J. Adekoya, et al., Advances in borophene: synthesis, tunable properties, and energy storage applications, Small 20 (40) (2024) 2403656.
[48] Y. Wang, et al., Design and innovative integrated engineering approaches based investigation of hybrid renewable energized drone for long endurance applications, Sustainability 14 (23) (2022) 16173.
[49] N.M. Jassim, et al., Plasmon assisted enhanced second-harmonic generation in single hybrid Au/ZnS nanowires, Opt. Mater. 64 (2017) 257–261.
[50] A. Mirdarsoltany, A.B. Dariane, M.I. Borhan, Comprehensive GIS-driven evaluation of drought severity and duration: comparative assessment of parametric and non-parametric SPI methodologies, Theor. Appl. Climatol. 156 (4) (2025) 225.
[51] A. Mirdarsoltany, et al., Linking land use change and hydrological responses: the role of agriculture in the decline of urmia lake, Hydrology 11 (12) (2024) 209.
[52] G. Zhou, et al., Multispectral camouflage and radiative cooling using dynamically tunable metasurface, Opt. Express 32 (7) (2024) 12926–12940.
[53] F. Alshaeer, et al., Synergistic defect passivation and charge transport enhancement via thiosemicarbazide-functionalized carbon nanotubes for high-efficiency lead-free $CsSnI_3$ perovskite solar cells: a pathway to 23.34 % efficiency, J. Alloys Compd. 1026 (2025) 180428.
[54] X. Liu, et al., Ultralight MXene/rGO aerogel frames with component and structure controlled electromagnetic wave absorption by direct ink writing, Carbon 230 (2024) 119650.
[55] Z.-Q. Wang, et al., Review of borophene and its potential applications, Frontiers of Physics 14 (3) (2019) 33403.
[56] M. Faraji, N. Arianpouya, NiCoFe-layered double hydroxides/MXene/N-doped carbon nanotube composite as a high performance bifunctional catalyst for oxygen electrocatalytic reactions in metal-air batteries, J. Electroanal. Chem. 901 (2021) 115797.
[57] S. Yuldasheva, et al., Enhanced tetracycline degradation in pharmaceutical wastewater via S-scheme photocatalysis using graphydine quantum dots/Janus MoSSe heterostructures, J. Water Proc. Eng. 68 (2024) 106470.
[58] J. Ye, et al., DFT+ U study on the magnetic properties of 3d transition metal doped β12 borophene, Phys. E Low-dimens. Syst. Nanostruct. 147 (2023) 115576.
[59] N. Alharbi, et al., Boosting efficiency and long-lifespan in perovskite solar cells via 2D-MXene/Janus MoSSe integration, J. Alloys Compd. 1013 (2025) 178501.
[60] F. Alshaeer, et al., Bandgap-engineered MXene-g-C3N4 interfacial layer for enhanced charge carrier dynamics in perovskite solar cells, J. Alloys Compd. 1011 (2025) 178247.
[61] H.A. Hasan, et al., Molecular design and synthesis of 3, 6-heterocyclic substituted carbazole with (D1-d-π-A) architecture for efficient dye-sensitized solar cell applications, J. Mol. Struct. 1337 (2025) 142122.
[62] K.A. Samawi, et al., Vertical growth of a 3D Ni-Co-LDH/N-doped graphene aerogel: a cost-effective and high-performance sulfur host for Li-S batteries, Phys. Chem. Chem. Phys. 26 (12) (2024) 9284–9294.
[63] K.A. Samawi, et al., MoS_2/graphdiyne nanotube/MXene 3D-interconnected ternary aerogel: a high-performance electrocatalyst for hydrogen evolution reaction, J. Solid State Chem. 334 (2024).
[64] W. Dizayee, et al., Synergistic effect of $Ni(OH)_2$ and MXene nanosheets in 3D framework on the improvement of dielectric, energy storage, mechanical and thermal characteristics of polyvinylidene fluoride(PVDF) polymeric composites, J. Alloys Compd. (2024) 1004.
[65] F. Parsaee, et al., Co-Fe dual-atom isolated in N-doped graphydine as an efficient sulfur conversion catalyst in Li-S batteries, J. Alloys Compd. 988 (2024) 174136.
[66] E. Abd-Alkuder Salman, et al., 3D hollow spheres comprising MXene/g-C_3N_4 Heterostructre for efficient polysulfide Adsorption and Conversion in high-performance Li-S batteries, J. Electroanal. Chem. (2023) 117629.
[67] M. Faraji, p. Derakhshi, k. tahvildari, Green and facile synthesis of graphene supported Pt nanoparticles for oxygen reduction reaction in polymer electrolyte fuel cells, Appl. Chem. 12 (45) (2017) 31–40.
[68] Akbarian, P., M. Kheirmand, and M. Faraji, Facile electrochemical fabrication of high-performance graphene quantum dots-supported Mn3O4/Ag hybrid catalyst for oxygen reduction reaction in alkaline media. Int. J. Energy Res. **n/a**(n/a).
[69] N.M. Jassim, Synthesis and nonlinear optical responses of Ag: ZnO core: shell nanoparticles induced by Z-scan technique, J. Opt. (2024) 1–10.
[70] L. Chai, et al., Tunable defects and interfaces of hierarchical dandelion-like NiCo2O4 via Ostwald ripening process for high-efficiency electromagnetic wave absorption, Chem. Eng. J. 429 (2022) 132547.
[71] M.H. Idan, R. Hassainn, M. Mohammed, Preparation and study of the effect of cobalt and magnesium on the structural and optical properties of cadmium sulfide compound, Journal of Nanostructures 12 (4) (2022) 921–931.
[72] M.H. Idan, R.G. Kadhim, M. Mohammed, Preparation and study of the effect of adding cobalt and magnesium on the morphological, optical properties and bacterial activity of cadmium sulfide compound, in: AIP Conference Proceedings, AIP Publishing, 2023.
[73] A. Afiqah-Idrus, et al., Deoxygenation of waste sludge palm oil into hydrocarbon rich fuel over carbon-supported bimetallic tungsten-lanthanum catalyst, Energy Convers. Manag. X 23 (2024).
[74] Mohammed, M.A., CoS THIN FILM DEPOSITED BY CHEMICAL SPRAY ENGINEERING TECHNIQUE: OPTICAL, GAS-SENSING AND STRUCTURAL CHARACTERISTICS.
[75] K. Wenelska, A. Dymerska, E. Mijowska, Promotion of borophene/NiO-based electrocatalyst for oxygen evolution reaction, Chem. Eng. J. 476 (2023) 146714.
[76] W. Mabhulusa, K.E. Sekhosana, X. Fuku, PdNiONF—Borophene nanocomposite as a promising catalyst for ethanol electro-oxidation reaction, Chemelectrochem 11 (12) (2024) e202400138.
[77] M.A. Mohammed, The effect of substrate temperature on the nanostructured V2O5 thin films, studying their structural, optical properties and testing as gas sensors, Journal of Nanostructures 15 (1) (2025) 200–209.
[78] B. Li, et al., UV and solar-based photocatalytic degradation of organic pollutants from ceramics industrial wastewater by Fe-doped ZnS nanoparticles, Chemosphere 336 (2023) 139208.
[79] H. Gharibi, M. Faraji, M. Kheirmand, The role of PANI/nafion on the performance of ORR in gas diffusion electrodes of PEM fuel cell, Electroanalysis 24 (12) (2012) 2354–2364.
[80] D. Tan, et al., Magnetic media synergistic carbon fiber@Ni/NiO composites for high-efficiency electromagnetic wave absorption, Chem. Eng. J. 492 (2024) 152245.
[81] K.A. Samawi, et al., Single-atom cobalt encapsulated in carbon nanotubes as an effective catalyst for enhancing sulfur conversion in lithium–sulfur batteries, Molecular Systems Design & Engineering 9 (5) (2024) 464–476.
[82] T. Shi, et al., Urchin -shaped NiO/Ni particles with a heterojunction deposited on porous carbon via electroplating and low-temperature heat treatment for efficient microwave absorption, Carbon 237 (2025) 120157.
[83] Y. Rao, et al., Flower-like NiO to flower-like NiO/Ni@C microspheres: an effective strategy to comprehensively improve the loss capabilities, J. Colloid Interface Sci. 629 (2023) 981–993.
[84] H. Yu, et al., Graphene/polyaniline nanorod arrays: synthesis and excellent electromagnetic absorption properties, J. Mater. Chem. 22 (40) (2012) 21679–21685.
[85] K. Gong, et al., Ultrathin carbon layer coated MXene/PBO nanofiber films for excellent electromagnetic interference shielding and thermal stability, Compos. Appl. Sci. Manuf. 176 (2024) 107857.
[86] Y. Chen, et al., Multiple Schottky contacts motivated via defects to tune the response ability of electromagnetic waves, Adv. Funct. Mater. (2025) 2417215.
[87] Q. Liu, et al., Fabrication of ultra-light nickel/graphene composite foam with 3D interpenetrating network for high-performance electromagnetic interference shielding, Compos. B Eng. 182 (2020) 107614.
[88] H. Rao, et al., Tailoring electromagnetic responsiveness of Tremella-like multi-dimensional heterostructures through a self-decomposition strategy, Chem. Eng. J. 500 (2024) 157121.
[89] R. Pei, et al., Anion doping as a "trigger" to modulate defect-tailored dielectric coupling for ultrathin microwave absorber, Small 21 (4) (2025) 2408538.
[90] D. Wu, et al., Enhanced interfacial polarization loss induced by hollow engineering of hollow alloyed CoFe-ZIF nanocages/carbon nanofibers for efficient microwave absorption, Inorg. Chem. Front. 12 (8) (2025) 3083–3097.
[91] R. Feng, et al., Multiphase magnetic array-anchored layered Fe3O4/FeO/C composites with magnetic coupling effect for highly efficient microwave absorption, Ceram. Int. 50 (24) (2024) 55461–55469.
[92] D. Wu, et al., Rational construction of mushroom-like Ni@ N-doped carbon tubes composites with enhanced electromagnetic wave absorption, J. Alloys Compd. 963 (2023) 171230.
[93] S. Hui, et al., Highly mixed index facet engineering induces defect formation and converts the wave-transmissive mott insulator NiO into electromagnetic wave absorbent, Adv. Mater. 37 (4) (2025) 2415844.
[94] B. Li, et al., NiO/Ni heterojunction on N-doped hollow carbon sphere with balanced dielectric loss for efficient microwave absorption, Small 19 (12) (2023) 2207197.
[95] H. Li, et al., Super magnetic loss induced by tunable damping coefficient through Ni nanoparticles size matching in magnetic carbon, Carbon 211 (2023) 118117.
[96] Y. Liu, et al., Enhanced microwave absorption properties of Ti 3 C 2 MXene powders decorated with Ni particles, J. Mater. Sci. 55 (2020) 10339–10350.
[97] S. Wang, W.-t. Xu, W. Ma, Preparation of MOFs-derived Ni/NPC materials and absorption properties, Mater. Lett. 362 (2024) 136205.
[98] X. Di, et al., Heterostructure design of Ni/C/porous carbon nanosheet composite for enhancing the electromagnetic wave absorption, Carbon 179 (2021) 566–578.

[99] L. Ma, et al., Facile synthesis of nitrogen-doped porous Ni@ C nanocomposites with excellent synergistically enhanced microwave absorption and thermal conductive performances, Carbon 201 (2023) 587–598.
[100] Z. Bi, et al., Experimental and theoretical study on broadband electromagnetic wave absorption of algae-like NiO/carbon nanotubes absorbers, J. Alloys Compd. 926 (2022) 166821.
[101] M. Shoeibi, et al., Improved IChOA-based reinforcement learning for secrecy rate optimization in smart grid communications, Comput. Mater. Continua (CMC) 81 (2) (2024).
[102] D. Wu, et al., Lightweight dielectric-magnetic synergistic necklace-shaped Co@ NCP/carbon nanofiber composites for enhanced electromagnetic wave absorption, Materials Today Nano 28 (2024) 100520.
[103] M. Motavaselian, et al., Diagnostic performance of magnetic resonance imaging for detection of acute appendicitis in pregnant women; a systematic review and meta-analysis, Archives of academic emergency medicine 10 (1) (2022) e81.
[104] X. Wang, et al., CoFe2O4/N-doped reduced graphene oxide aerogels for high-performance microwave absorption, Chem. Eng. J. 388 (2020) 124317.
[105] F. Hu, et al., Tailoring electromagnetic responses of delaminated Mo2TiC2Tx MXene through the decoration of Ni particles of different morphologies, Chem. Eng. J. 440 (2022) 135855.
[106] J. Yan, et al., The 3D CoNi alloy particles embedded in N-doped porous carbon foams for high-performance microwave absorbers, Carbon 152 (2019) 545–555.